Indian Geotech J (February 2020) 50(1):96–116
https://doi.org/10.1007/s40098-019-00388-0

ORIGINAL PAPER

Measurement and 2D Axisymmetric Modeling of Mining Blast-Induced Ground Vibrations

Imad Kadiri[1] · Younès Tahir[1] · Saïf ed-Dîn Fertahi[2] · Omar Iken[1] · Maryam Dlimi[1] · Rachid Agounoun[1] · Khalid Sbai[1]

Received: 28 March 2019 / Accepted: 6 September 2019 / Published online: 18 September 2019

Abstract Blast-induced ground vibrations are considered as an undesirable phenomenon resulting from productivity explosions in the extractive industries. Moreover, they are considered as a high potential cause for the damage of the surrounding structures. In this paper, the ground vibration data were recorded using a seismograph device at different distances from the detonation point in the quarry site of "*Sococim Cement Factory*," which is located on Senegal. Thereafter, 2D axisymmetric numerical model has been established to simulate the propagation of the mechanical shock wave in the considered medium. The numerical modeling was developed under *AUTODYN* software, which is an explicit FEM code. First of all, the numerical model has been validated against the experimental measurements, by comparing the numerical and experimental longitudinal (V_l) and vertical (V_v) velocity signal at different gauges, for different equivalent explosive charges per delay ($m_{eq(TNT)}$). A calibration was carried out only on the elastic properties of the rock to achieve this purpose. The adjusted values of K and G allowed to reproduce the numerical PPVs, in order to be in a good agreement with the measured PPVs. The energy dissipation due to the RHT model and the phenomenon of vibration's damping as a function of time at the gauges locations is well reproduced by the numerical model. It is noted that the plasticity and damage near the borehole have no effect on the propagation celerity of the shock wave, which remains the same in the elastic medium. Furthermore, the damaged zone nearby the detonation point has been assessed and described by identifying the transition of limestone properties from the elastic–plastic to plastic-damage state. The characterization of the damaged zone, near the borehole for different explosive charges per delay, helps to calculate the face burden side and to enhance the blasting design.

✉ Imad Kadiri
imad_kadiri@hotmail.com

[1] Laboratoire d'Etude des Matériaux Avancés et Applications (LEM2A), Ecole Supérieure de Technologie de Meknès, Université Moulay Ismail (UMI), Km 5, route d'Agouray, N6, 50040 Meknes, Morocco

[2] École Supérieure de Technologie de Fès, Université Sidi Mohamed Ben Abdellah (USMBA), Route d'Imouzzer, BP 2427, Fes, Morocco

Graphic Abstract

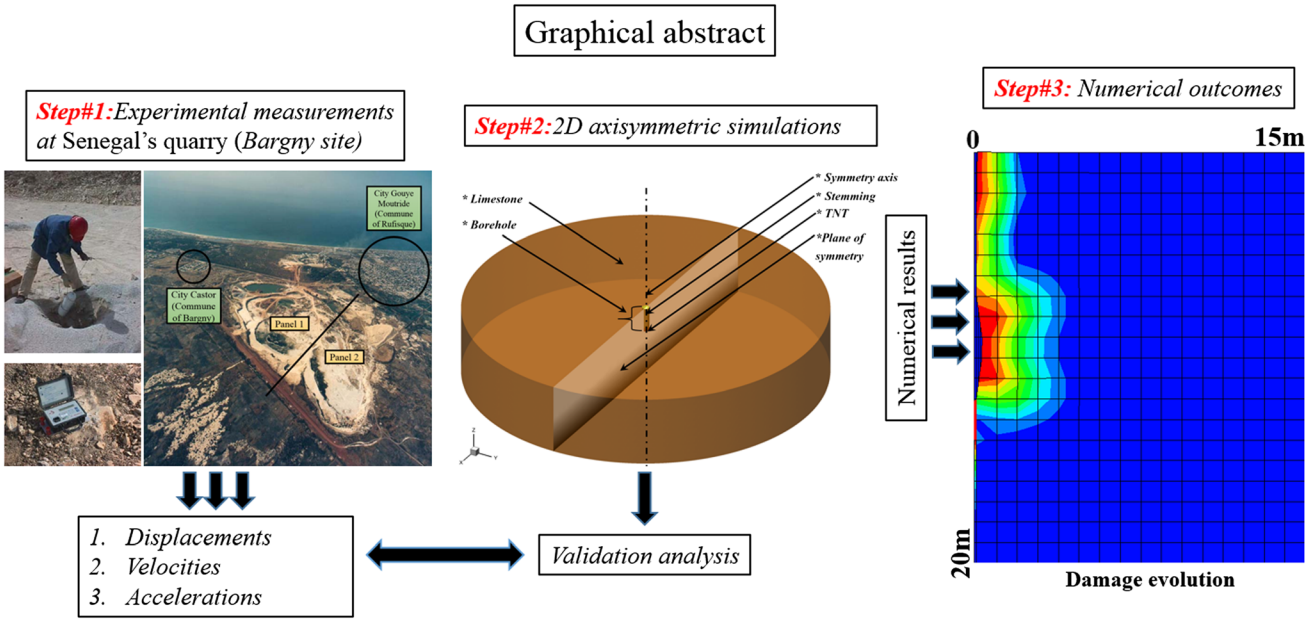

Keywords BIGVs · Experimental measurements · FEM · 2D axisymmetric modeling · RHT model

List of Symbols

C	Porous sound speed (m/s)
C_L, C_T	Longitudinal and transversal celerities (m/s)
C_s	Bulk sound speed (m/s)
e	Internal energy (J)
ef_{min}	Minimum strain to failure
E	Young modulus (kPa)
$\mathbf{f}$	Vector of external force (N)
$f_{c,el}$	Elastic compressive strength (MPa)
$f_{t,el}$	Elastic tensile strength (MPa)
f_c	Uniaxial compressive strength (MPa)
f_s	Shear strength (MPa)
f_t	Uniaxial tensile strength (MPa)
G	Elastic shear modulus (kPa)
I	Identity tensor
K	Elastic bulk modulus (kPa)
L	Length (m)
L_{TNT}	Length of TNT (m)
$m_{eq(TNT)}$	Equivalent mass of TNT (kg)
N	Compaction exponent
p	Pressure (Pa)
p_{comp}	Solid compaction pressure (Pa)
p_{el}	Initial compaction pressure (Pa)
t	Time (s)
U_x, U_y	Mechanical displacements (m)
$\mathbf{v}$	Velocity vector (m/s)
V_l, V_v	Longitudinal and vertical velocities (m/s)
$Y_{elastic}$	Yield surface
Y_{fail}	Failure surface
Y_{fric}	Residual friction resistance surface

Greek Symbols

γ	Ratio of specific heats
μ	Dynamic viscosity (Pa.s)
ν	Poisson coefficient
ρ	Density (kg/cm^3)
ρ_0	Initial density (kg/cm^3)
ρ_{TMD}	Theoretical maximal density (kg/cm^3)
σ	Total Cauchy stress tensor (kPa)
α	Porosity parameter
α_{int}	Initial porosity
θ	Lode angle
Γ	Grüneisen parameter
$\frac{\rho_{matrix}}{\rho_{porous}}$	Additional state variable
$\dot{\epsilon}$	Strain rate

Abbreviations

BIGVs	Blast-induced ground vibrations
PPV	Peak particle velocity
FEM	Finite element method
RHT	Riedel, Hiermaier and Thoma

Introduction

Background of the Research

The mechanical characterization of blast waves is an attracting topic for the companies and design offices that perform production blasts in quarries, such as cement plants [12], phosphate production, or public companies that lead public works in building sites for the infrastructure design such as roads, bridges [21].

Up to now, and according to the exhaustive bibliographic research that our team have carried out, several experimental and numerical studies on the propagation of the blast waves were conducted on concrete structures such as bridges, dams [36] and on metallic structures [30] as lattice structures [32] and plates [37, 38]. It has been concluded from this state-of-the-art synthesis that most of the considered blasts are carried out in the air medium [16, 23]; hence, the shock wave is transmitted to the assessed structure. Regarding the numerical studies, the design's dimensions of the studied configurations do not generally exceed $10 \times 10 \times 10$ m^3 [28]. Therefore, even though the numerical studies are performed on these structures, the numerical computations are not enough costly in terms of the calculation time and allocated material resources [27]. These structure designs of reduced dimensions do not allow to appreciate the attenuation of the shock wave with the distance. This phenomenon is essential to characterize the possible damages on the structures distant from the blasts [5].

Recently, our research team conducted a blast experimental study in *Senegal*, namely at the "*Sococim cement factory*" presented in Fig. 1. In fact, this quarry site has been the subject of several unitary and production blasts, and the components of the velocity, in addition to the acoustic pressure, were measured and recorded using a seismograph and a microphone. In order to promote the achieved experimental results, an axisymmetric two-dimensional numerical model has been proposed in order to afford, with accuracy, the experimental results recorded in terms of the longitudinal (V_l) and vertical (V_v) velocities at the specific measuring points and for well-defined blast equivalent TNT loads, namely 50 kg, 100 kg and 150 kg (Table 4).

The present numerical contribution is considered important, since the numerical studies conducted until now are mostly 2D planar [15, 40] or 3D [17, 19]. In addition, they shed light on small-scale industrial applications. Otherwise, the numerical study that is presented in this paper would simulate a unitary shot in a limestone site, of real dimensions, which extends on a diameter of 1200 m and a depth of 100 m. The equivalent charge of the explosives ($m_{eq(TNT)}$) was confined with stemming that was modeled as non-cohesive sand material, and the shock blast waves are directly transmitted to the limestone.

State of the Art of Blast-Induced Ground Vibration (*BIGV*) Studies

Xiaohua et al. [38] carried out numerical simulations to assess the effects of close proximity underwater explosion on the nonlinear dynamic behavior (damage processes) of concrete gravity dams including orifices. As a first step, the authors calibrated their coupled model using experimental test data, in order to provide accurate and reliable simulation results. This research team showed that a tighten orifice's gate would notably decrease the damage level of the gravity dam. Moreover, the dam with orifice is vulnerable to close proximity underwater explosion compared to the configuration of the dam without orifice.

Fig. 1 **a** Location of "*Sococim cement factory*." **b** Location of commune of Bargny and Rufisque

Numerical simulations of blasting-induced fracture expansion in coal masses have been performed by Zhao et al. [37] using *LS-DYNA* software. Firstly, the authors used Kachanov equation, besides the crack connections to evaluate the damage zone, which is located at the tip of bedding. Secondly, they assessed the propagation of the blasting-induced fracture, through the analysis of the bedding plane effect on the reflection and transmission of blasting stress waves. In addition, this research team assessed the effect of the delay time [34] on the crack initiation between two adjacent boreholes.

Zhang et al. [36] carried out finite element (*FE*) analysis using *ABAQUS/Explicit* program to evaluate the nonlinear structural responses of an arch dam subjected to underwater explosion (*UNDEX*) shock loading. The authors identified two failure modes of the arch dam, namely the tensile cracking of the dam base concrete and the break-off failure of the monolith, which is located next to the explosive source. Moreover, they showed that the computational strategy of *ABAQUS/Explicit* software is time efficient and helps to achieve accurate results that are relatively undemanding in time.

A numerical modeling for blast-induced fragmentation in sublevel caving (SLC) mines has been conducted by Changping et al. [34] using the *LS-DYNA* code. In fact, according to these authors, drilling and blasting have an impact on the flow of SLC material. They showed that a finer fragmentation could be achieved if a long delay time is defined. In addition, the authors discussed the main limitations that are related to the numerical modeling. Table 1 presents a summary of some numerical studies conducted on *BIGVs*.

Numerical models require the definition of several parameters, such as the mechanical properties of the medium and its heterogeneity, cracking, water flow, etc., that are difficult to determine. As a result, several authors tend to characterize BIGVs using empirical and statistical laws. Zeng et al. [35] carried out a regression analysis, using the empirical formula of Sadovsky [33], of the wave propagation based on the field monitoring data, in order to control the blast-induced rock damage near the Fangchenggang nuclear power station located in China. Indeed, it is essential to control the blast-induced effects to ensure an engineering safety of nearby buildings. The

Table 1 Summary of some numerical studies conducted on *BIGVs*

Authors	Approach	Studies	Main findings and results
Hu et al. [9]	Numerical investigations with *AUTODYN*	Blast loading model of the RC column under close-in explosion induced by the double end initiation explosive cylinder	Application of an accurate blast loading model under close-in explosion induced by the double-end-initiation explosive cylinder considering D/L ratio and evaluation of the scaled distance using the test data and numerical calculations
Zhi et al. [39]	Experimental and numerical analysis with *ANSYS/LS-DYNA*	Experimental and numerical investigations of a single-layer reticulated dome subjected to external blast loading	Validation of the numerical elastic and inelastic strain results of the multi-curved shell against the experimental measurements. Examination of strain, plasticity development and the absorbed energy by each component of the multi-curved shell. Identification of elastic vibrations, slight damage, local failure and global collapse of the multi-curved shell
Esmaeili et al. [5]	Finite element calculation with *LS-DYNA*	Finite element method simulation of explosive compaction in saturated loose sandy soils	Multiple small charges with detonation delays would enhance EC effectiveness. An increased compaction and a decreased heave are achieved for charges placed on the lower half of the soil layer. Using more charge weight would enhance both surface heave and compaction of the lower layers
Linforth et al. [16]	Experiment and numerical investigations with *LS-DYNA*	Unsaturated soil blast: flying plate experiment and numerical investigations	Numerical validation of *LS-DYNA* models throughout a series of soil blast tests with 0.5 kg TNT charges that were carried out on different plate sizes. The sensitivity of the soil properties generally affects the variations in the plate height
Saleh et al. [27]	Numerical analysis with *LS-DYNA*	Evaluation of soil and fluid structure interaction in blast modelling of the flying plate test	Assessment of the softening behavior of semi-cohesive prairie soils due to the development of pore pressure and the cohesion angle decrease
Tang et al. [32]	Explicit finite element numerical simulations with *LS-DYNA*	Numerical simulation of a cable-stayed bridge response to blast loads, part I: model development and response calculations	Examination of the damage mechanism and severity of the bridge tower, pier and deck due to blast loads from 1000 kg TNT explosion, which is located at 0.5 m from the bridge tower and pier and to 1 m above the deck

authors derived a satisfactory relationship that has been calibrated further between the peak particle velocity (*PPV*), located at a distance of 30 m away from the borehole and the charge per delay time, in order to design the blast. Consequently, they presented interesting results that help to take control of the blast-induced damage of rock mass.

The blast-induced rock mass damage around tunnels has been assessed by Verma et al. [33]. It is noted that the empirical correlation used by the authors has been previously validated against ultrasonic tests performed on rock core samples. This research team conducted field studies on five tunnels located in India and Himalaya to study the generated blast-induced damage, depending on a wide range of the mass quality (Q) values. Besides, other parameters involved in the blast-induced damage were considered in their study, such as the specific charge, the perimeter charge factor, the maximum charge per delay, the advancement and confinement factors. One hundred and thirty three experimental blast results were collected and analyzed by the authors, in order to develop an empirical correlation, which is helpful to evaluate the rock mass damage.

Murmu et al. [20] carried out empirical and probabilistic analysis of BIGVs. The authors collected 640 blast data, concerning different rock types from different quarry sites located in Turkey and India. They validated the accuracy of the empirical model for peak particle velocity (PPV) that takes into consideration the burden and maximum charge per delay. Moreover, this research team performed probabilistic analysis using Monte Carlo (MC) simulations and they show that the PPV follows a lognormal distribution. Moreover, BIGV assessment using various estimation models has been conducted by Ongen et al. [22]. The authors monitored the results from 22 trial blasts to produce 39 vibration measurements, which have been recorded at a residential area located at 396 m from the blasting point. It should be noted that these authors used several standards to evaluate the harmful effect of vibration, such as USBM criterion [4], Ambraseys Hendron, Langefors Kihlstrom and Indian Standards.

Aim of the Research

The main aim of this paper is to develop a two-dimensional axisymmetric modeling that would approach the experimental results that we achieved on the "*Sococim site*" located in Senegal. Firstly, a series of unit trial blast tests were conducted in the "*Sococium cement factory*." The longitudinal, vertical and transverse velocities' signals were recorded on three sites, in particular, the site (a): "*Panel 1* (*upper exploitation level*)," the site (b): "*Conveyor belt*" and finally the site (c): "*Macodo's house*" which is located at city Castor bargny. Subsequently, a two-dimensional axisymmetric model was established for three unit blasts, namely 50 kg, 100 kg and 150 kg (Table 4); thus, the numerical results were compared to the experimental results to conclude on the accuracy and validity of the numerical modeling. The numerical modeling is extremely useful and helps to describe the damaged zone, at the vicinity of the borehole for different explosive charges per delay, which helps to calculate the face burden side and to enhance the blasting design.

Experimental Investigations at the "*Sococim Cement Factory*"

Site Description

The site of "*Sococim*" is located on *Senegal* (Fig. 1a), some thirty kilometers from *Dakar*. It is situated between two villages, the commune of "*Bargny*" in the northwest and the commune of "*Rufisque*" in the south (Fig. 1b). On the "*Rufisque*" side, the "*Gouye Mouride*" district is located at the limit of the factory, more than a kilometer from the quarry. This workers' city is built on blue marls and limestone. The city of "*Sococim*" is located on the *Bargny* side. "*Sococim*" is relatively close to the blasting carried out at Panel 1 (about 600 m). The site of "*Bargny*" consists of three lithological units that are described as shown in Fig. 2 (from bottom to top).

1. In depth, a gray homogeneous limestone, formed by multi-levels with thicknesses ranging from 30 to 60 cm approximately. Its overall thickness is 8 m. This level is based on blue marls that form the bedrock of the deposit. Its average thickness is 10 m.
2. A yellow limestone, which contains silex, with 5 m of thickness intercalation of limestone and marls. This level ensures the transition between the aforementioned limestone level and the surface marl level
3. A level of marls presenting some beds of limestone that are decreasing toward the east until disappearing

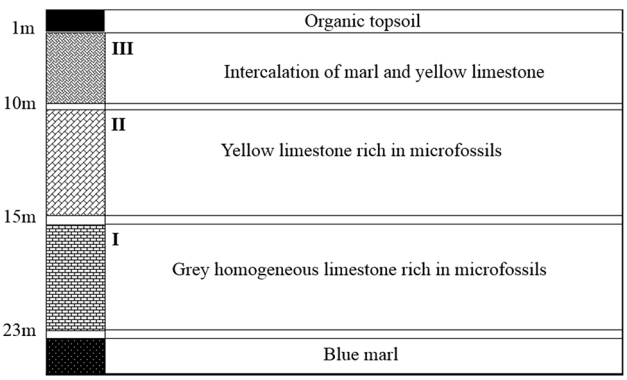

Fig. 2 Geology of the "Sococim cement factory"

Fig. 3 **a** "*Sococim cement factory*." **b**, **d** Drilling of TNT filling inside the boreholes. **c** "Mini seis" device

4. Finally, on the surface, one meter of organic topsoil

Figure 3a presents the "*Sococim quarry*," which is the subject of the experimental study. In addition, Fig. 3b, d shows the integration of the explosive in the boreholes by the operators. Moreover, "*Mini seis*," presented in Fig. 3c, has been used to record the seismic data (vertical, longitudinal, transverse velocities, displacements and accelerations). The parameters of a signal that are measured by a tridirectional seismograph are related to the characteristics of its sensors. The relative position of the seismic tridirectional seismograph with respect to the source determines the azimuth and dip of the seismic ray emerging at the station; hence, the signal is decomposed into three components. The tridirectional seismograms allow to study the polarization's directions of the seismic signal in space. In an isotropic homogeneous medium the P wave is polarized in the direction of propagation, which is called the longitudinal direction (*L*). On the other hand, the S wave can be polarized in two directions perpendicular to that of the P wave (transverse and vertical) as presented in Fig. 4. The technical characteristics of this device are shown in Table 2 [10].

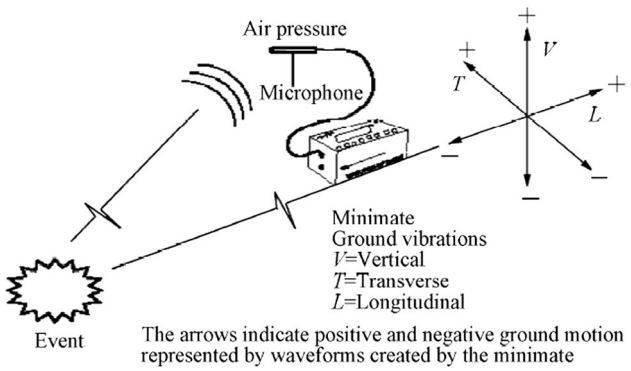

Fig. 4 Measure of the vertical, longitudinal, transverse velocities by tridirectional seismograph [1]

Table 2 Technical specifications of "*Mini seis*" measuring device [10]

Acquisition	2048 information/lane/second
Storage	Storing records on internal memory
Duration of registration	4 s
Triggering seismic acquisition	By exceeding the minimum threshold of the sensors
Tridirectional geophones	4.5 Hz electronically corrected at 2 Hz

Aim and Methodology

The blasts were made using 105, 115, 165 and 200 mm diameter drill boreholes with a depth varying between 7.5 and 11 m. Electrical delay detonators were located at the bottom of the boreholes in order to initiate the blasts. The boreholes corresponding to the trial blasts (*TB*) were charged with "*Dynaroc 6 90/3150*" and "*Nitram TX9 130/5000*" (Table 3).

Table 3 Theoretical parameters of the explosives [3]

	Dynaroc 6 A	Nitram 9
Gas volume (0 °C/1 At) (L/kg)	893	857
Total mass energy (MJ/kg)	4.5	4.2
Total volume energy (MJ/L)	6.4	5
Detonation pressure (confined) (ϕ 80 mm) (GPa)	13.6	13.5
Detonation temperature (°C)	–	2227
Velocity of detonation (m/s)	–	6200

The trigger thresholds were set from 0.4 to 2 mm/s depending on the distance from the detonation point and the unit load of the explosive that is used. In fact, this threshold is defined as the lowest value compatible with the level of ambient vibrations (background noise). Indeed, it is desirable that the device records only the vibrations created by the detonation and not by other events, for instance road traffics, crushers, etc., which could by caused by the human activities in the surrounding area.

Experimental Results

Experimental measurements were performed on several sites as it is shown in Fig. 5. Three sites were considered to validate the two-dimensional axisymmetric numerical modeling, in particular, the site (a): "*Panel 1* (*upper exploitation level*)," the site (b): "*Conveyor belt*" and the site (c): "*Macodo's house*," which is located at city Castor Bargny. The experimental measurement of longitudinal, vertical and transverse velocities at the considered sites is shown in Table 4.

Numerical Modeling

AUTODYN is an explicit *FEM* code, commonly used to model nonlinear dynamics of solids, fluids, gas and their interaction [15]. It fact, this software has been widely used, because of its capability to study the explosion and blasting problems [40]. Moreover, the *AUTODYN's* material library is composed of several explosives and the users can define their associated material properties, for instance, rock material conveniently.

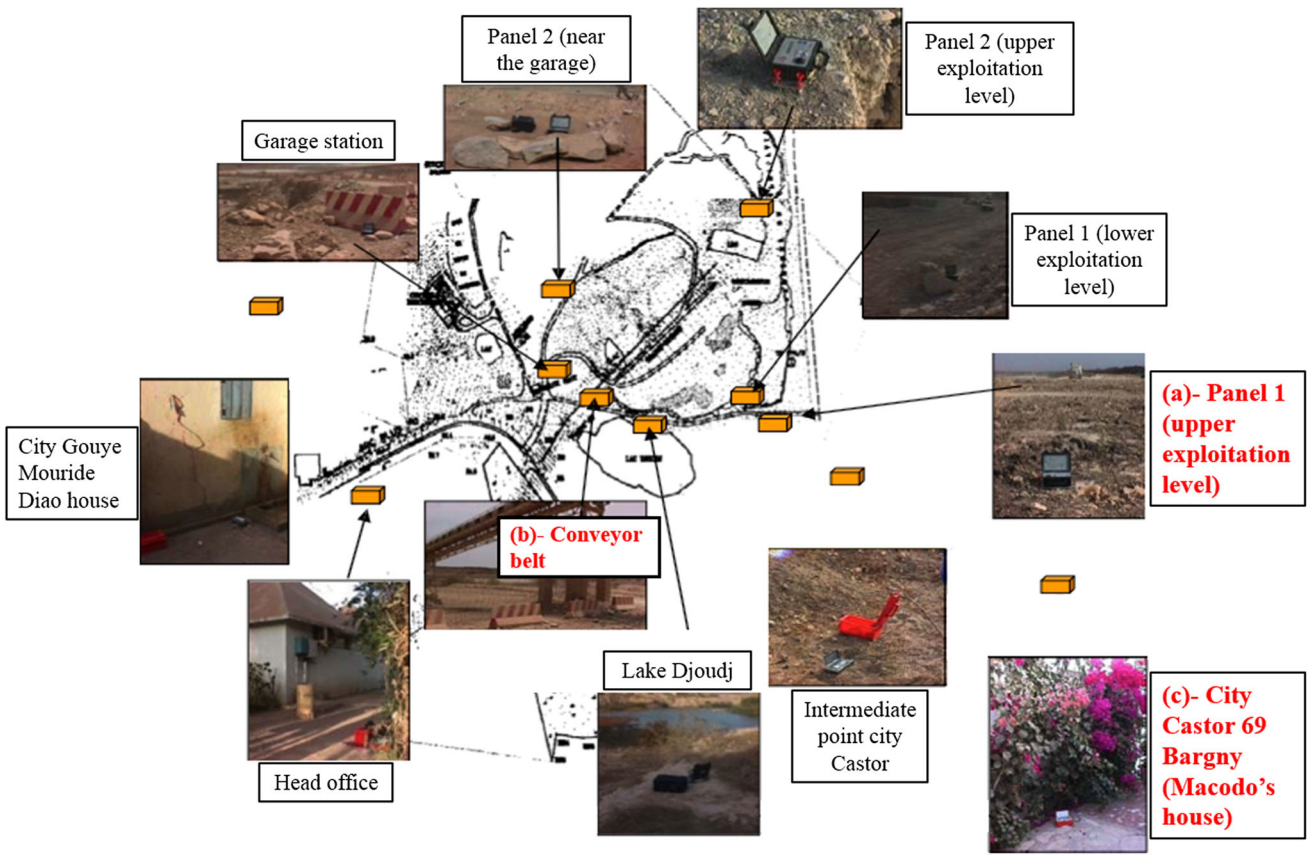

Fig. 5 Location of the considered sites: **a** Panel 1 (upper exploitation level). **b** Conveyor belt. **c** City Castor (Macodo's house)

Table 4 Experimental measurement of longitudinal, vertical and transverse velocities at the considered sites

Trial blast	Measuring points	Measurement distance (m)	Maximal charge per delay (kg)	Sensor ID	Velocities (mm/s)			
					Longitudinal	Vertical	Transverse	Maximal
Num #1	P1 (upper bearing)	150	50	139	13	13.84	8.25	13.84
	Conveyor belt	436		653	5.34	13.97	3.87	13.97
	Macodo	540		1318	8.25	7.49	2.79	8.25
Num #2	P1 (upper bearing)	77	100	139	42.67	25.91	25.91	42.67
	Conveyor belt	469		653	2.48	6.98	2.35	6.98
	Macodo	406		1318	6.86	9.27	2.54	9.27
Num #3	P1 (upper bearing)	82	150	139	48.26	39.62	25.4	48.26
	Macodo	455		1318	6.1	8.54	3.43	8.54
	Conveyor belt	458		653	2.16	6.35	2.41	6.35

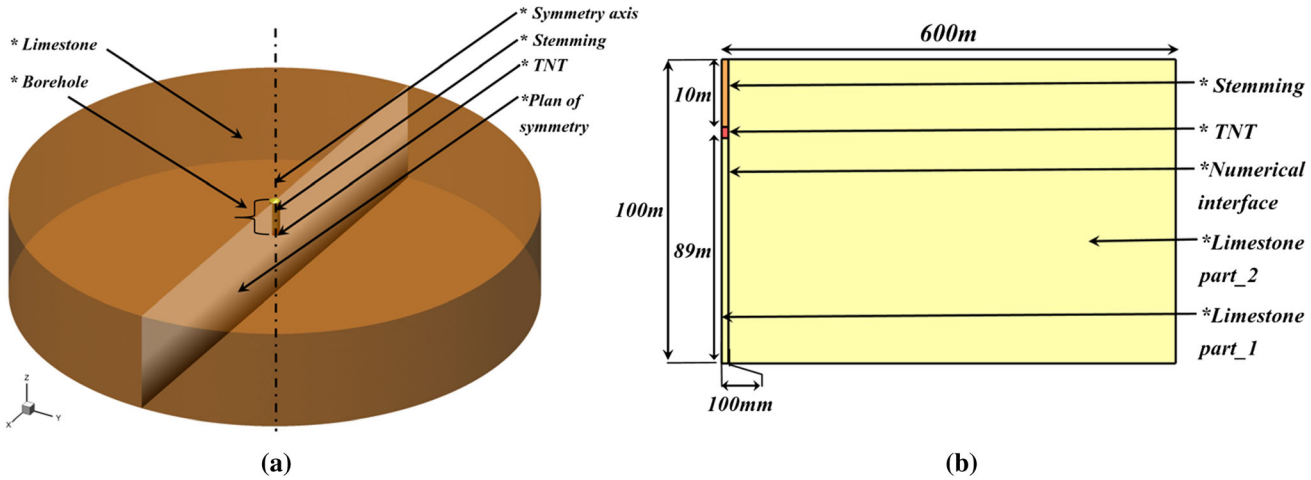

Fig. 6 **a** Three-dimensional section of the quarry field, showing the cutting plane, which divides the TNT borehole in half. **b** Two-dimensional axisymmetric section of the quarry field ($m_{eq(TNT)}$)

Figure 6a presents a 3D design of the quarry site. The explosion of an equivalent weight charge of TNT ($m_{eq(TNT)}$) is located at the middle center of the limestone field. The quarry site has a diameter of 1200 m and a depth of 100 m. Given the shape of the limestone field and since the drilling axis and the axis of the equivalent weight of the TNT explosive belong to a symmetry plan; thus, it was decided to conduct two-dimensional axisymmetric numerical studies instead of a three-dimensional study, which would be very expensive in terms of the computational time and hardware resources to use in order to validate the experimental results [5].

The topography of the site is relatively flat; hence, the topographic survey was not taken into account during the geometrical modeling (Fig. 6a). Accordingly, the upper limit of the geometrical model has been designed horizontally. The medium has been considered homogenous and isotropic. The existing discontinuities (joints, fractures, bedding plane, etc.) were not taken into account. The axisymmetric model that has been used to validate the experimental study and to simulate the propagation of the blast wave is presented in Fig. 6b. The drilling depth is 11 m, and its diameter is 200 mm. The length of the explosive (L_{TNT}) is calculated using Eq. 1.

$$L_{TNT} = \frac{4m}{\rho\pi\phi^2} \tag{1}$$

where $m_{eq(TNT)}$ is the equivalent mass of TNT. For instance, one meter has been used to insert 50 kg of the equivalent weight of the TNT explosive, having a radius of 100 mm, while 10 m was considered as enough to confine the explosive with the stemming as shown in Table 5.

AUTODYN was used to create the two-dimensional axisymmetric model, for the mesh generation, as well as for the resolution of the physical problem formulation. An Eulerian domain was first created on *AUTODYN*, with the following dimensions 100×600 m^2, above which two Lagrangian fields were defined. The Lagrangian domains are, respectively, characterized by the following dimensions 100×599.90 m^2, 89×0.1 m^2 as shown in Fig. 6b.

Table 5 Stemming and explosives length corresponding to different equivalent TNT charges

TNT equivalent charge per delay (kg)	Length of drilling 11 m/diameter of drilling 200 mm	
	Stemming's length (m)	Explosive's length (m)
≅ 50	10	1
≅ 100	9	2
≅ 150	8	3

Subsequently, both of the Lagrangian fields were joined together to create a single limestone body. Hence, there is a need to define a numerical interface between these two solid limestone fields. The interface between the two parts is numerical, and the relative displacement between them is zero. The numerical interface is a solid contact zone that has been created to join the two limestone solid domains. The advantage of this geometric creation by part is to generate a structured mesh, on which the size of the meshing elements can be easily modified.

AUTODYN is convenient to use when it comes to creating simple two-dimensional geometries, but it has a huge insufficiency and does not allow the designer to create more complex geometries, having complicated details. In addition, the rectangular Eulerian area 11×0.1 m^2 was filled in two stages: first, to integrate the equivalent mass of TNT explosive; and second, to confine it by the stemming material.

Eulerian Formulation

The Navier–Stokes equations, for a Newtonian viscous fluid, associated with the state equations are integrated in time with the boundary conditions, in order to provide a single solution for the flow of the explosion's products [23]. A major simplification has been considered in this numerical analysis, because cracking and water flow were not taken into account while establishing the numerical model. It must be emphasized that the time step is divided into a Lagrangian step and an advection step.

Continuity Equation

Continuity equation is expressed using Eq. 2 [28].

$$\frac{\partial \rho}{\partial t} + \nabla.(\rho \mathbf{v}) = 0 \tag{2}$$

Momentum Equation

Momentum equation is expressed as presented in Eq. 3 [28].

Table 6 Parameters of *TNT* explosive [2]

EOS JWL	
Parameter A (kPa)	3.74E+08
Parameter B (kPa)	7.74E+06
Parameter R1	4.15
Parameter R2	0.9
Parameter W	0.35
C-J detonation velocity (m/s)	6.93E+03
C-J energy/unit volume (kJ/m^3)	6.00E+06

$$\frac{\partial \rho \mathbf{v}}{\partial t} + \nabla.(\rho \mathbf{v} \otimes \mathbf{v}) = \nabla.\bar{\bar{\sigma}} + \mathbf{f} \tag{3}$$

where ρ is the density, $\mathbf{v}$ is the flow velocity vector of the Eulerian material (air, TNT), $\mathbf{f}$ is defined as the vector of externally applied loads. $\bar{\bar{\sigma}}$ is the total Cauchy stress tensor that is defined in Eq. 4 [28].

$$\bar{\bar{\sigma}} = -p\bar{\bar{I}} + \mu \nabla \mathbf{v} + \nabla \mathbf{v} \tag{4}$$

In Eq. 4, p is the pressure, $\bar{\bar{I}}$ is the identity tensor, and μ is the dynamic viscosity.

Energy Equation

The energy equation is expressed in Eq. 5. E is the total energy, which is the sum of the internal and kinetic energies [28].

$$\frac{\partial \rho E}{\partial t} + \nabla.(E\mathbf{v}) = \bar{\bar{\sigma}} : \nabla \mathbf{v} \tag{5}$$

Jones–Wilkins–Lee (JWL) State Equation of TNT

The state equation of TNT is expressed using Eq. 6. In addition, the parameters that are used for the JWL state equation of TNT are presented in Table 6 [14]. V is the specific volume of TNT, and it is expressed as follows ($V = \frac{\rho_0}{\rho}$).

$$p = A\left(1 - \frac{\omega}{R_1 V}\right)e^{-R_1 V} + B\left(1 - \frac{\omega}{R_2 V}\right)e^{-R_2 V} + \frac{\omega}{V}E \tag{6}$$

State Equation of Air Material

The state equation of air is expressed in Eq. 7.

$$p = (\gamma - 1)\frac{\rho}{\rho_0}E \tag{7}$$

where γ is the ratio of the specific heats of air material. The physical properties of air are listed in Table 7.

Table 7 Physical properties of air [2]

EOS AIR	
Parameters	Values
Reference density (ρ_0) (g/cm^3)	0.001225
Gamma (γ)	1.4

State Equation of Stemming

The mechanical properties of stemming were based on the granular material model, implemented into *AUTODYN* [2]. This material model was developed to describe the compaction of a porous material.

The EOS compaction is described by a plastic compaction curve, which is given as a piecewise linear curve with ten points, namely the density as a function of pressure, as shown in Fig. 7a. The solid "asymptote" to this curve is linear (Eqs. 8, 9).

if $\rho = \rho_{\mathrm{TMD}}$

$$P = 0 \tag{8}$$

if $\rho \geq \rho_{\mathrm{TMD}}$

$$P = c_s^2(\rho - \rho_{\mathrm{TMD}}) \tag{9}$$

where ρ_{TMD} is the theoretical maximum density (no porosity left), c_s is the bulk sound speed of fully compacted material.

The elastic loading/unloading compaction curve is given by the density-dependent bulk sound speed, $c(\rho)$ as expressed in Eq. 10.

$$P = c^2(\rho).\rho \tag{10}$$

The density-dependent bulk sound speed, $c(\rho)$, was given as a piecewise linear curve of ten pairs, as shown in Fig. 7b.

Lagrangian Formulation (RHT Model)

Equation of State

The equation of state of the Mie–Grüneisen form is used to relate the pressure (p) to the density and the internal energy (e), for the fully compacted material (Eq. 11).

$$p(\rho, e) = A_1\eta + A_2\eta^2 + A_3\eta^3 + \Gamma\rho e \tag{11}$$

$$\eta = \frac{\rho}{\rho_0} - 1 \tag{12}$$

In compression ($\eta \geq 0$) (Eq. 12), the equation of state is parameterized as a third-order polynomial with the following parameters A_1, A_2, and A_3, while in extension ($\eta \leq 0$), only a linear dependence on the compression η with the same parameter A_1 is used [2]. In addition, the path to full compaction has been considered by introducing a porosity parameter α [7]. Hence, the porosity parameter α is determined by the initial porosity α_{int}, the compaction exponent (N) and two limiting pressure values, i.e., the initial compaction pressure p_{el} and the solid compaction pressure p_{comp} (Eq. 13). These parameters determine under which pressure the pores begin to collapse and when they are fully compacted, respectively.

$$\alpha = 1 + (\alpha_{\mathrm{init}} - 1)\left[\frac{p_{\mathrm{comp}} - p}{p_{\mathrm{comp}} - p_{\mathrm{el}}}\right]^N \tag{13}$$

Hereby, Γ is the Grüneisen parameter, ρ the current density, and ρ_0 the initial density. By the introduction of the porosity α and $\frac{\rho_{\mathrm{matrix}}}{\rho_{\mathrm{porous}}}$ as an additional state variable, the compaction of the pores in the material and the compaction work that comes along with this permanent deformation can be included in the equation of state (Eq. 14).

$$p = f(\rho_{\mathrm{matrix}}, e) \longrightarrow (\mathrm{porous})\, p = f(\rho\alpha, e) \tag{14}$$

Figure 8 illustrates this pore compaction path in a pressure (p) versus density (ρ) plot. After the initial

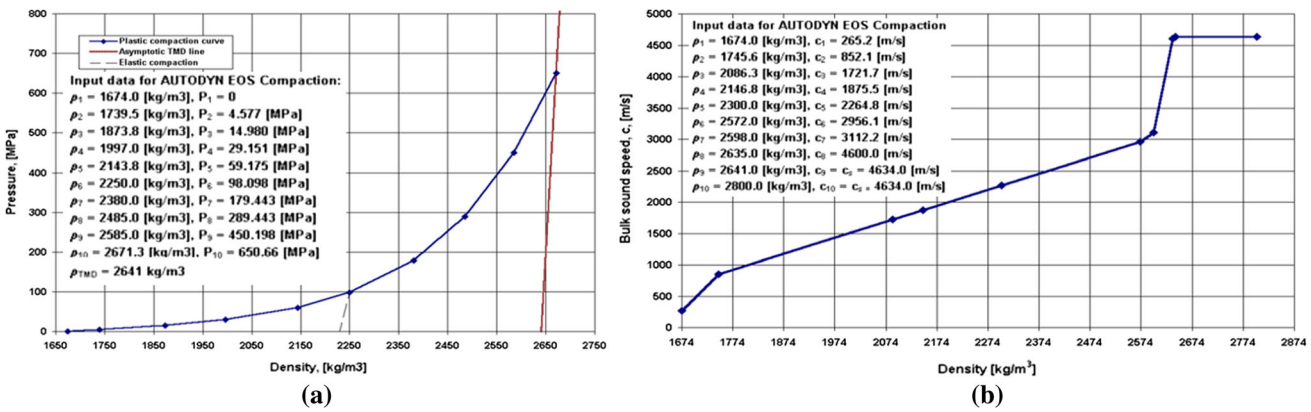

Fig. 7 **a** The plastic compaction curve for pressures. **b** Input data for the density-dependent bulk sound speed [13]

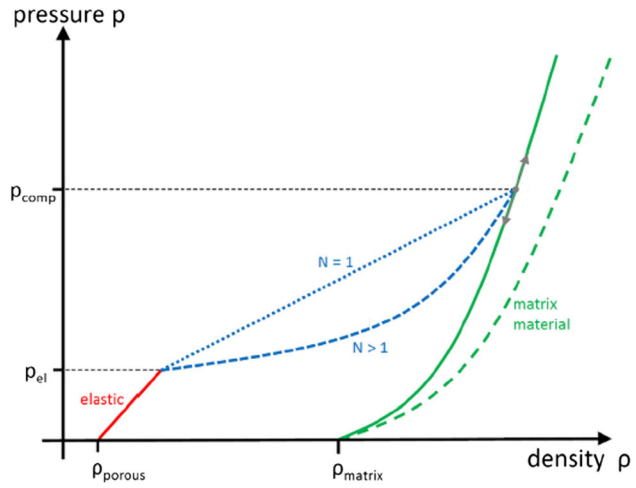

Fig. 8 Schematic explanation of the pore compaction loading path and its parameters. The green dashed curve describes the solid equation of state of the matrix material, which differs from the fully compacted porous material (solid green line). In blue, two different compaction paths due to a variation of the compaction exponent N are displayed [29] (color figure online)

compaction pressure p_{el} is exceeded, the pores collapse according to the path (blue curves) defined by the compaction exponent (N) and the solid compaction pressure p_{comp}. At higher pressures, the green dashed curve describes the solid equation of state of the matrix material, which is different from the fully compacted porous material (solid green line).

Failure Surface

Eqs. 15 and 16 define the equivalent stress σ_{eq} and the hydrostatic pressure p as a function of the principal stresses σ_1, σ_2 and σ_3, respectively, for general load cases.

$$\sigma_{eq} = \sqrt{\frac{1}{2}[(\sigma_1-\sigma_2)^2+(\sigma_2-\sigma_3)^2+(\sigma_3-\sigma_1)^2]} \tag{15}$$

$$p = -\frac{1}{3}(\sigma_1+\sigma_2+\sigma_3) \tag{16}$$

The strength model was proposed and developed in [24–26]. Figure 9a, b shows the three surfaces describing the elastic limit Y_{el}, failure Y_{fail} and residual shear strength Y_{fric} of the damaged concrete under confined conditions.

The failure surface Y_{fail} is described by Eq. 17 and presented in Fig. 9a, b. The compressive meridian $Y^*_{TXC}(p)$ (Eq. 18) describes the pressure dependence for principal stress conditions ($\sigma_1 < \sigma_2 - \sigma_3$) (tensile stresses defined positive) with parameters A and N. All measures of hydrostatic pressure and the deviatoric strength are normalized over the uniaxial compressive strength f_c, when denoted with (*).

$$Y_{fail}(p,\theta,\dot{\epsilon}) = Y_{TXC}(p)R_3(\theta)F_{Rate}(\dot{\epsilon}) \tag{17}$$

for $p^* \geq \frac{1}{3}$

$$Y^*_{TXC} = A(p^* - \mathrm{HTL}'^*)^n \tag{18}$$

for $p^* < \mathrm{HTL}^*$

$$Y^*_{TXC} = 0 \tag{19}$$

Rotation of the compressive meridian around the hydrostatic axis spans the complete failure surface in stress space. To describe reduced strength on shear and tensile meridians, it is multiplied with a factor $Q_2 \leq R_3(\theta) \leq 1$. The lode angle θ describes stress triaxiality and depends on the third invariant J_3 of the stress tensor (Eq. 20). The dimensionless function R_3 (Eq. 21) scales referring to the compressive meridian Y_{TXC} with $R_3 \leq 1$. The ratio Q_2 of tensile to compressive

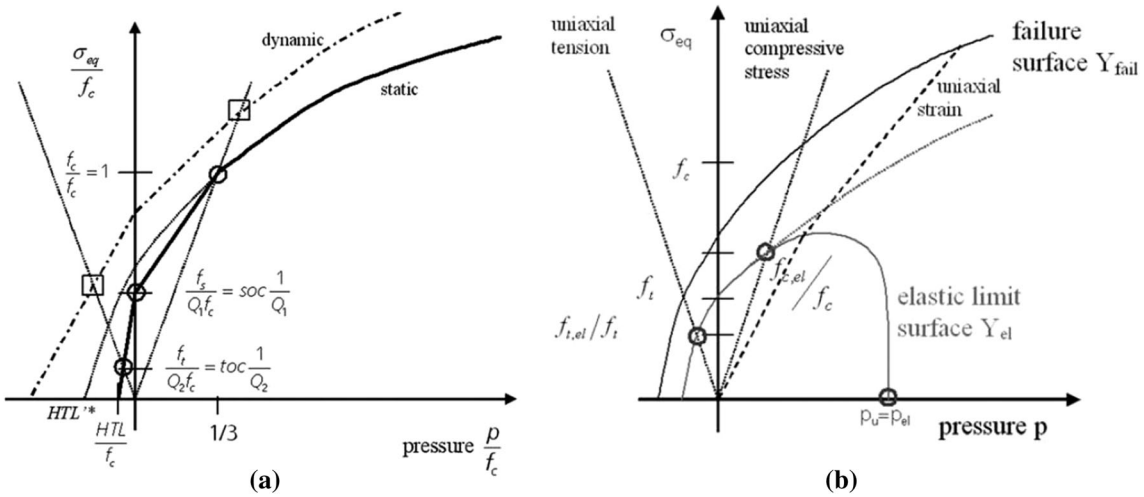

Fig. 9 **a** Three surface concepts for the concrete strength with hardening, failure and residual friction resistance [6]. **b** Surface concept for the concrete strength with failure and residual friction resistance [25]

meridian decreases with increasing pressure. This effect is called "brittle to ductile transition" and is described by Eq. 22.

$$\cos(3\theta) = \frac{3\sqrt{3}}{2}\frac{J_3}{J_2^{\frac{3}{2}}} \tag{20}$$

$$R_3(\theta, Q_2) = \left[\frac{[2(1-Q_2^2)\cos(\theta) + (2Q_2-1)]}{\times[4(1-Q_2)^2\cos^2(\theta) + 5Q_2^2 - 4Q_2]^{\frac{1}{2}}} \over {4(1-Q_2^2)\cos^2(\theta) + (1-2Q_2)^2}\right] \tag{21}$$

$$0.5 < Q_2 = Q_{2,0} + Bp^* \leq 1 \tag{22}$$

The term $F_{\text{Rate}}(\dot{\epsilon})$ in Eq. 17 accounts for the rate enhancement of deviatoric strength. Eqs. 23–32 present an empirical fit functions for uniaxial tensile and compressive loading. Strain rate enhancement factors F_{Rate} between these limits are linearly interpolated.

In compression

if $\dot{\epsilon} \leq 30\text{s}^{-1}$

$$F_{\text{Rate}} = \frac{f_{\text{cd}}}{f_{\text{c}}} = \left(\frac{\dot{\epsilon}}{\dot{\epsilon_0}}\right)^{\alpha} \tag{23}$$

if $\dot{\epsilon} > 30\text{s}^{-1}$

$$\frac{f_{\text{cd}}}{f_{\text{c}}} = \gamma\dot{\epsilon}^{\frac{1}{3}} \tag{24}$$

$$\dot{\epsilon_0} = 30 \times 10^{-6}\text{s}^{-1} \tag{25}$$

$$\alpha = \frac{1}{5 + \frac{3}{4}f_{\text{c}}} \tag{26}$$

$$\log(\gamma) = 6\alpha - 0.492 \tag{27}$$

In tension

if $\dot{\epsilon} \leq 30\text{s}^{-1}$

$$F_{\text{Rate}} = \frac{f_{td}}{f_{\text{t}}} = \left(\frac{\dot{\epsilon}}{\dot{\epsilon_0}}\right)^{\delta} \tag{28}$$

if $\dot{\epsilon} > 30\text{s}^{-1}$

$$\frac{f_{td}}{f_{\text{t}}} = \eta\dot{\epsilon}^{\frac{1}{3}} \tag{29}$$

$$\dot{\epsilon_0} = 3 \times 10^{-6}\text{s}^{-1} \tag{30}$$

$$\delta = \frac{1}{10 + \frac{1}{2}f_{\text{c}}} \tag{31}$$

$$\log(\eta) = 7\delta - 0.492 \tag{32}$$

Elastic Limit and Hardening

The initial elastic surface Y_{elastic} of the virgin material is expressed by Eq. 33. The elastic scaling function F_{elastic} takes the value $f_{\text{t,el}}/f_{\text{t}}$. Above $f_{\text{c,el}}/3f_{\text{c}}$ it is equal to $f_{\text{c,el}}/f_{\text{c}}$. Between these bonds, it is linearly interpolated with respect to the pressure. $f_{\text{t,el}}, f_{\text{c,el}}$ are the elastic tensile and compressive stress, respectively.

The elastic surface is closed consistently with the porous equation of state toward higher pressures involving pore compaction using a parabolic cap function F_{cap} (Eq. 34).

Between the initial elastic surface and the ultimate failure surface hardening is described using Eqs. 35, 36.

$$Y_{\text{elastic}} = Y_{\text{fail}}F_{\text{elastic}}F_{\text{cap}} \tag{33}$$

$$F_{\text{cap}} = \begin{cases} 1 & p \leq p_u = \frac{f_{\text{c}}}{3} \\ \sqrt{1 - \left(\frac{p - p_u}{p_0 - p_u}\right)^2} & p_u < p < p_0 \\ 0 & p \geq p_0 = p_{\text{el}} \end{cases} \tag{34}$$

$$Y_{\text{hard}} = Y_{\text{elastic}} + \frac{\epsilon_{\text{eq}}^{\text{pl}}}{\epsilon_{\text{eq}}^{\text{pl,hard}}}(Y_{\text{fail}} - Y_{\text{elastic}}) \tag{35}$$

$$\epsilon_{\text{eq}}^{\text{pl,hard}} = \frac{(Y_{\text{fail}} - Y_{\text{elastic}})}{3G}\left(\frac{G_{\text{elastic}}}{G_{\text{elastic}} - G_{\text{plastic}}}\right) \tag{36}$$

Damage Evolution and Residual Surface

When hardening states reach the ultimate strength of the concrete on the failure surface Y_{fail} damage is accumulated during further inelastic loading controlled by plastic strain. The model by Holmquist et al. [8] is taken as basis for the evolution law. Eqs. 37 and 38 specify how the plastic increments are normalized over the effective strain to failure $\epsilon_{\text{eq}}^{\text{pl,fail}}$. The effective strain to failure is depending on the hydrostatic pressure p with the shape parameters D_1, D_2 and a lower limit ef_{min}. The effect of damage is modeled as a loss in deviatoric strength by interpolating between the failure surface Y_{fail} and residual friction resistance surface Y_{fric} (Eqs. 39 and 40).

$$D = \int_{\epsilon_{\text{eq}}^{\text{pl,hard}}}^{\epsilon_{\text{eq}}^{\text{pl,fail}}} \frac{1}{\epsilon_{\text{eq}}^{\text{pl,fail}}(p)} d\epsilon_{\text{eff}}^{p} \tag{37}$$

$$\epsilon_{\text{eq}}^{\text{pl,fail}}(p^*) = D_1(p^* - \text{HTL}^*)^{D_2} \geq ef_{\text{min}} \tag{38}$$

$$Y_{\text{fric}} = B.p^m \tag{39}$$

$$Y_{damaged} = Y_{\text{fail}} + D(Y_{\text{fric}} - Y_{\text{fail}}) \tag{40}$$

All the above input parameters are summarized in Table 8.

Boundary Conditions

The boundary conditions applied to the two-dimensional axisymmetric model are shown in Fig. 10. The symmetry axis condition has been applied to the left boundary of the

Table 8 Standard input parameters of the "RHT concrete 35-MPa" (*AUTODYN* [2])

EOS CONC-35MPA (*P alpha*)	
Reference density (g/cm^3)	2.75
Porous density (g/cm^3)	2.314
Porous sound speed (m/s)	2.92E+03
Initial compaction pressure (kPa)	2.33E+04
Solid compaction pressure (kPa)	6.00E+06
Compaction exponent	3.00E+00
EOS CONC-35MPA (*Polynomial*)	
Bulk modulus A1 (kPa)	3.53E+07
Parameter A2 (kPa)	3.96E+07
Parameter A3 (kPa)	9.04E+06
Parameter (Γ)	1.22
Reference temperature (K)	3.00E+02
Specific heat (J/kg K)	6.54E+02
Strength RHT concrete	
Shear modulus (kPa)	1.67E+07
Compressive strength (f_c) (kPa)	3.50E+04
Tensile strength (f_t/f_c)	0.1
Shear strength (f_s/f_c)	0.18
Intact failure surface constant (A)	1.6
Intact failure surface exponent (n)	0.61
Tens./comp. meridian ratio ($Q_{2,0}$)	0.6805
Brittle to ductile transition (B)	0.0105
G (elas.)/(elas.-plas.)	2
Elastic strength/f_t	0.7
Elastic strength/f_c	0.53
Fractured strength constant (B)	1.6
Fractured strength exponent (m)	0.61
Failure RHT concrete	
Damage constant (D_1)	0.04
Damage constant (D_2)	1
Minimum strain to failure	0.01
Residual shear modulus fraction	0.13

limestone field, because of the geometric symmetry with respect to the (x).

Boundary conditions have been applied to the Eulerian field as well as to the Lagrangian field. The mechanical displacements on the bottom and right edges of the Lagrangian field have been blocked, respectively, along both of (x) and (y) axes. Moreover, a transmission condition of the mechanical wave has been applied on the bottom and right boundaries of the Lagrangian field, in order to avoid their reflection into the rock mass field. Furthermore, an outflow boundary condition has been applied on the three boundaries of the Eulerian field.

Figure 11 presents the geometric location of the gauges (numerical monitors) that were used to plot the longitudinal and vertical velocities recorded experimentally on the quarry site using a seismograph. Three gauges were defined on the top border of the Lagrangian field. For instance, the monitors are located, respectively, with respect to the symmetry axis at the following distances: 82 m, 455 m and 458 m as shown in Fig. 11c for $m_{eq(TNT)} = 150$ kg.

Mesh Sensitivity Analysis

The mesh of the limestone and air field have been defined Lagrangian and Eulerian meshing, respectively [9]. In fact, this approach is well reviewed and checked in numerical simulations under *AUTODYN* [9] or *LS-DYNA* software [39]. Figure 12a shows a progressive quadrilateral grid that has been generated for the Eulerian field, while Fig. 12b shows a structured quadrilateral grid of the Lagrangian domain, with an equidistant step of discretization. It is necessary to define an Eulerian domain in order to simulate the blast wave. Otherwise, no pressure will be generated in the Lagrangian field after detonating the explosive. Indeed, the Eulerian domain ensures the propagation of TNT, as well as the stemming, which is used for its confinement in the air.

A progressive mesh must be generated around the equivalent mass of the explosive, since its propagation velocity is high. Therefore, a compromise between the time step and the space step must be ensured to reproduce the physical phenomenon of detonation and transmission of the pressure wave toward the Lagrangian field. The total number of elements that has been generated is 240,089 elements. Concerning the Eulerian domain, the following discretization has been adopted: 100*1200 divisions, 100 divisions for the horizontal axis and 1200 divisions for the vertical axis. The first two arrays adjacent to the TNT each have an edge length along the vertical axis of 100 mm, and subsequently, a progressive mesh factor is automatically applied by *AUTODYN* to discretize the Eulerian domain along the vertical axis into 1200 divisions.

The horizontal axis of the Lagrangian field has been discretized by 100 divisions (one cell every 1 m), moreover it has been meshed along the vertical axis into 1200 divisions (one cell every 0.5 m). It remains to be known that the numerical part of the Lagrangian domain, which is collinear with the drilling of the TNT was meshed by 89 divisions (one element every 1 m) along the horizontal axis and by one meshing element in the vertical direction, having an edge's length of 100 mm.

The mesh sensitivity study is an important step in the numerical studies, because it ensures the independence of the achieved numerical results with respect to the spatial discretization [36]. Four grids were assessed during this mesh sensitivity study, namely G_1 grid with 60,022 elements, G_2 grid with 120,044 elements, G_3 grid with

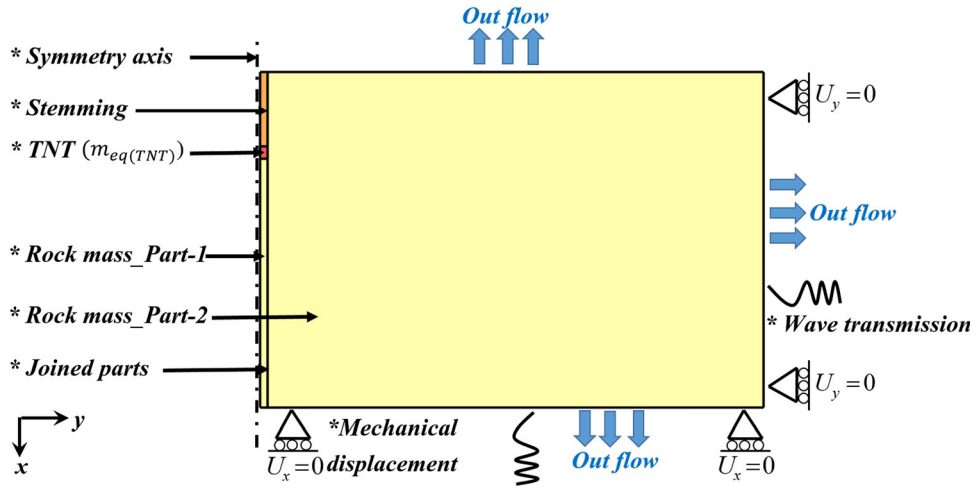

Fig. 10 Boundary conditions for the two-dimensional axisymmetric quarry field

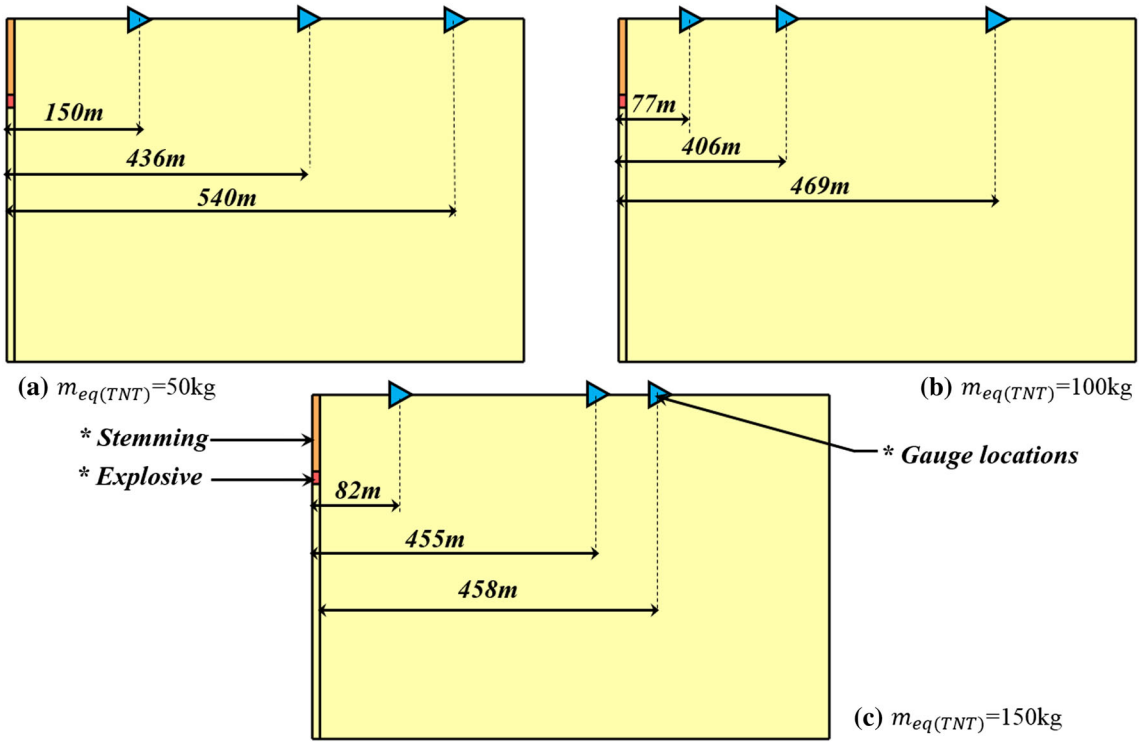

Fig. 11 Location of the measurement points regarding the initial position of the TNT borehole. **a** $m_{eq(TNT)} = 50$ kg, **b** $m_{eq(TNT)} = 100$ kg, **c** $m_{eq(TNT)} = 150$ kg

240,089 elements and G_4 grid with 360,134 elements. Longitudinal PPV has been defined as the convergence criterion. It is noted that the results that correspond to G_3 grid are very close to the results of G_4 grid. In fact, a slight difference of 2% has been noted. However, the difference between the results of G_3 and G_2 remain greater than 10%. In addition, it is noted that the damping of longitudinal velocity signal that not occur for coarse meshes, namely G_2 and G_1 mesh grids (Fig. 13). As a conclusion, the mesh that has been used to carry out the numerical analysis consists of 240,089 elements divided as previously described (Fig. 12).

Results and Discussion

Validation of the Numerical Model

Three trial blasts were carried out in this numerical study. Each trial blast's borehole has got the following

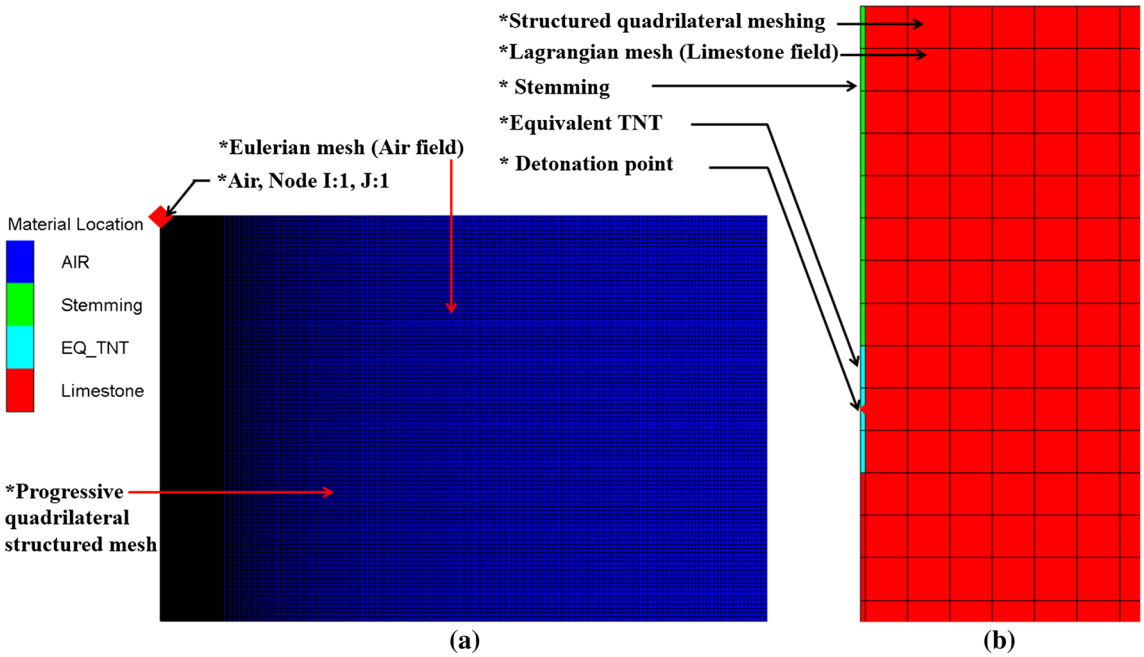

Fig. 12 **a** Eulerian mesh for the air field. **b** Lagrangian mesh for the limestone field

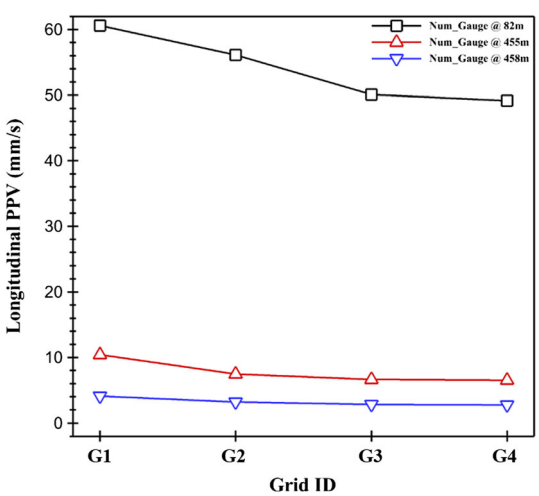

Fig. 13 Mesh sensitivity and convergence test results

specifications: a diameter of 200 mm and a depth of 11 m. The boreholes were filled by 50 kg, 100 kg and 150 kg of TNT charge starting from their bottom section, which corresponds, respectively, to 1, 2 and 3 m of the TNT's length. The main purpose of this modeling is to reproduce the orders of PPV at different distances from the blast and to assess the damaged zone around it.

In this paper, the rock mass was assumed to have the same mechanical behavior as the concrete, through the RHT model. This model is characterized by several parameters that are difficult to adjust. The validation analysis was achieved by comparing the evolution of longitudinal (V_l) and vertical (V_v) velocities as a function of time at different gauges as presented in Figs. 14, 15, 16 and 17.

The calibration was carried out on the elastic properties of the rock mass. Poisson's ratio was fixed at $v = 0.3$ and Young modulus (E) was calibrated, so that the numerical results would be in good agreement with the experimental measurements. Finally, the retained value is $E = 7 \times 10^7$ kPa, which implies that $K = 5.8 \times 10^7$ kPa and $G = 2.7 \times 10^7$ kPa.

Based on the previous tuned parameters (K and G), it has been found that the longitudinal and vertical PPV of the numerical results are close to those of the experimental measurements for the equivalent TNT charges ($m_{eq(TNT)} = 150$ kg and 100 kg) at the assessed gauge points, as it is presented in Table 9 and Figs. 14, 15, 16 and 17.

In addition, the phenomenon of vibration's damping as a function of time and the gauges locations is well reproduced by the numerical model. In fact, Figs. 14, 15, 16 and 17 show that the damping pattern of the numerical velocities is in a good agreement with the experimental measurements. For instance, for a TNT charge of 150 kg and for the gauge located at 455 m, both of the numerical and experimental vibrations are damped after approximately 1.25 s (Fig. 15). The formulation of the RHT model is able to reproduce a physical damping due to the modeling of dissipative energy phenomena, which is a characteristic of the nonlinear response of the rock related to the plasticity with hardening and damage. It is worth to say that even an elastic medium subjected to a brief dynamic

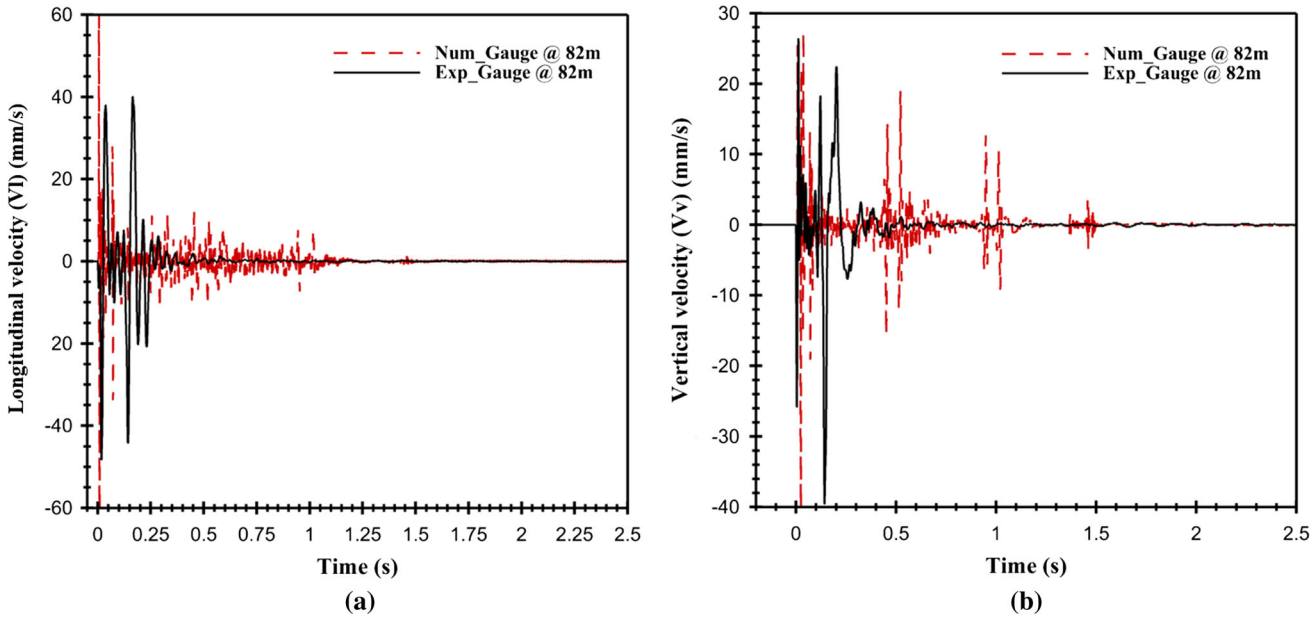

Fig. 14 Comparison between the numerical and experimental longitudinal (**a**) and vertical velocities (**b**) at $y = 82$ m $m_{eq(TNT)} = 150$ kg

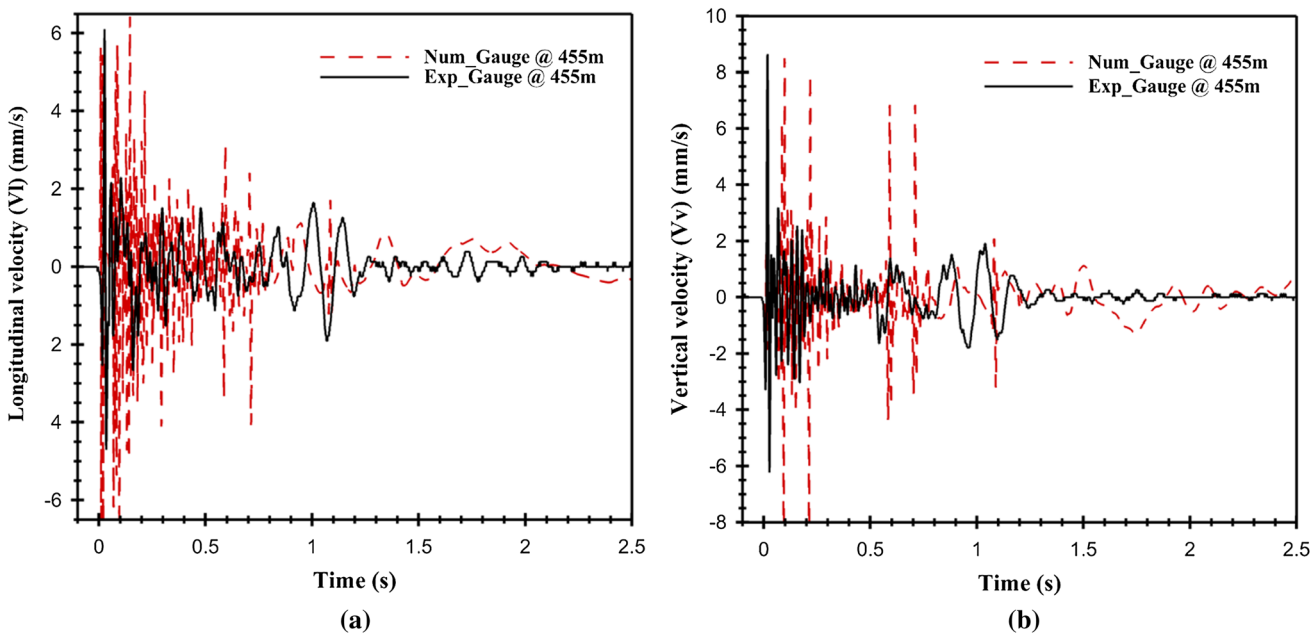

Fig. 15 Comparison between the numerical and experimental longitudinal (**a**) and vertical velocities (**b**) at $y = 455$ m for $m_{eq(TNT)} = 150$ kg

load tends to reach an equilibrium state, which indicates the effect of other sources of damping. For a linear analysis, these sources are modeled by an elastic damping, for example Rayleigh damping (mass and stiffness-weighted damping) [31]. It is also possible to combine, in the same analysis, the physical damping from nonlinear modeling and a global damping from a structural model that takes into account, without any explicit distinction, many sources of energy dissipation. However, the global damping from a structural model has not a clear physical basis, and the amount of energy they dissipate is difficult to control during numerical analyzes [11]. In our case, the attenuation of vibrations induced by the shock wave are well reproduced only by using the physical damping of RHT model, without introducing any additional damping.

The influence of other parameters on longitudinal and vertical PPV, namely the uniaxial compressive strength (f_c), uniaxial tensile strength (f_t) and shear resistance (f_s), has been carried out. For instance, Table 9 presents the results obtained for different values of the uniaxial

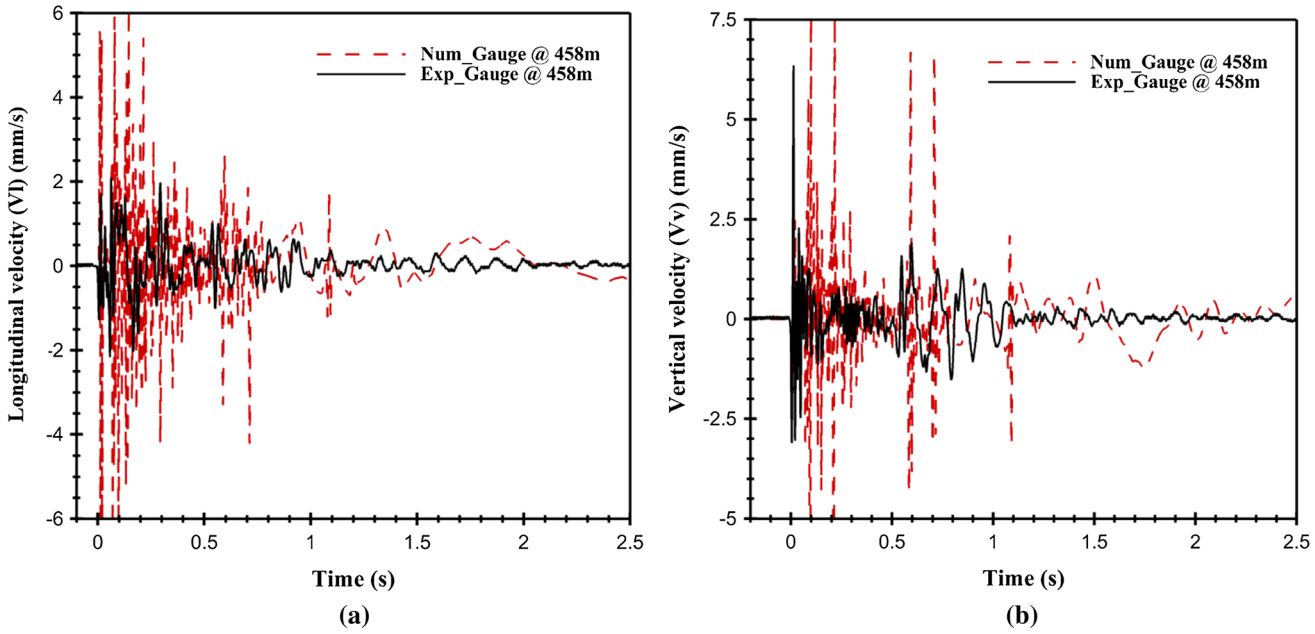

Fig. 16 Comparison between the numerical and experimental longitudinal (**a**) and vertical velocities (**b**) at y = 458 mm for $m_{eq(TNT)} = 150$ kg

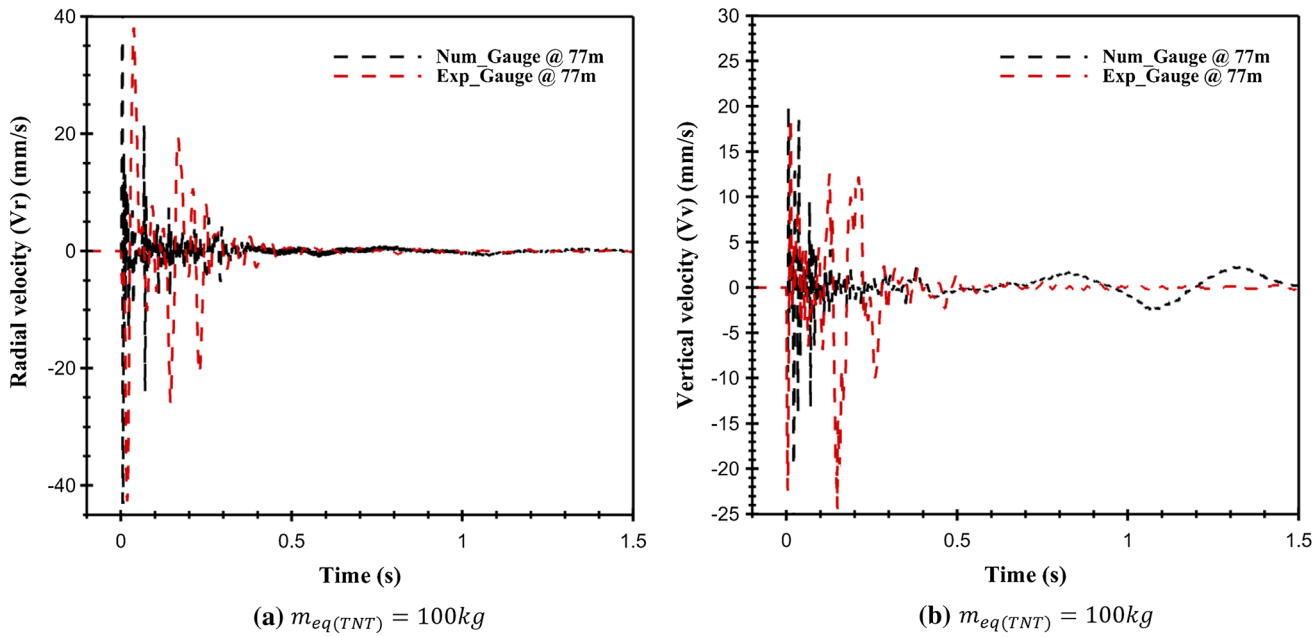

Fig. 17 Comparison between the numerical and experimental longitudinal (**a**) and vertical velocities (**b**) at y = 77 m for $m_{eq(TNT)} = 100$ kg

compressive strength (f_c). It was found that the PPVs values are very close for an f_c ranging from 20 to 100 MPa. Similar results were found for the other parameters mentioned above (f_t and f_s). In this case, and since the gauges are located far from the blast, an equivalent elastic model could be sufficient to reproduce the recorded PPV measurements [18]. However, the energy of the blast should be dissipated by an elastic damping model, because the rock mass does not include any physical damping. Nevertheless, such analysis is not appropriate to predict the modified properties of the medium (damaged zone around the blast). In fact, the damage presents for us a major interest, because it provides useful information regarding the design pattern of production blasts (a discussion is presented further in the "Evaluation of the Damaged Zone Around the Blast" section).

Concerning the temporal distribution, it is difficult to reproduce the signal's frequencies. The numerical signal presents higher dominant frequencies compared to the experimental signal. This difficulty of reproducing the

Table 9 Numerical results for different values of the uniaxial compressive strength (f_c) and experimental measurements of the longitudinal and vertical PPV for the gauges located at 82 m, 455 m and 458 m

		Gauges located		
		@ 82 m	@ 455 m	@ 458 m
Experimental results	Longitudinal PPV (mm/s)	48.26	6.1	2.16
Numerical results	Longitudinal PPV (mm/s)			
$f_c = 20$ MPa		49.37	6.77	2.5
$f_c = 35$ MPa		50.09	6.63	2.83
$f_c = 50$ MPa		51.13	6.8	2.72
$f_c = 100$ MPa		51.66	6.91	2.64
Experimental results	Vertical PPV (mm/s)	39.62	8.45	6.35
Numerical results	Vertical PPV (mm/s)			
$f_c = 20$ MPa		26.82	7.77	7.58
$f_c = 35$ MPa		26.51	8.48	6.12
$f_c = 50$ MPa		26.27	7.68	7.72
$f_c = 100$ MPa		24.76	7.4	6.94

Table 10 Comparison between the wave detection time using numerical simulations (RHT modeling of rock mass) and using analytical formula in an elastic medium

Trial blast	Maximal charge per delay ($m_{eq(TNT)}$) (kg)	Gauge location (m)	Wave detection time (t_1) using analytical formula (elastic modeling of rock mass) (s)	Wave detection time (t_2) using numerical simulations (RHT modeling of rock mass) (s)	Relative error (%)
Num #1	50	150	0.03031972	0.03283	8.27
		436	0.08812933	0.09996	13.42
		540	0.1091510	0.12495	14.47
Num #2	100	77	0.01556412	0.01568	0.74
		406	0.08206538	0.09261	12.84
		469	0.09479967	0.10731	13.19
Num #3	150	82	0.016574	0.0165	0.45
		455	0.091969	0.102	10.90
		458	0.09257	0.102	10.17

temporal signal has been encountered in several numerical studies conducted with *AUTODYN* and *LS-DYNA* software [37, 39]).

Wave Celerity Assessment for the Elastic and RHT Model

The seismograph is triggered only from a certain threshold for which the shock wave reaches the measuring points. In the current case, the threshold corresponds to an interval of 0.4–2 mm/s. However, the numerical simulation is estimating the time duration (t) that is required to reach these points. This time duration corresponds to the detection of the longitudinal wave, which is the fastest. As shown in Figs. 14, 15, 16 and 17, a shift to the origin ($t = 0$ s) has been applied to the numerical signal, in order to be compared with the experimental recording. Hence, the wave's detection time, which is obtained numerically at the measurement points is not represented in these figures. Table 10 presents a comparison between the wave detection time using numerical simulations (RHT modeling of rock mass) and using analytical formula for the longitudinal celerity (C_L) (Eq. 41) in an elastic medium.

$$C_L = \sqrt{\frac{K + \frac{4G}{3}}{\rho}} \tag{41}$$

The relative error between the analytical time (t_1) and the numerical time (t_2) was evaluated for three equivalent TNT loads per delay ($m_{eq(TNT)}$) and for three gauges as presented in Table 10. For the gauges that are within the first 100 m from the trial blast, the relative error is practically negligible. For instance, for $m_{eq(TNT)} = 100$ kg at the gauge located at 77 m from the blast, the relative error is 0.74%

and for $(m_{eq(TNT)}) = 150\,kg$ at the gauge located at 82 m from the blast, the relative error is 0.45%. Otherwise, the relative error increases with the distance. For instance, for $(m_{eq(TNT)}) = 50\,kg$ at the gauge located at 150 m from the trial blast, the relative error is 8.27%. It can be concluded from these results that the velocity propagation of the shock waves is the same within a linear elastic medium. The amplified relative error for the gauges, which are located at a distance greater than 100 m, is purely numerical due to the mesh grid refinement. It can be concluded that the RHT does not affect the celerity of the wave, which was slightly equivalent to the wave's celerity calculated analytically under the assumption of an elastic medium.

Evaluation of the Damaged Zone Around the Blast

The performed numerical simulations represent a trial blast designed with a single borehole without a free face. Figure 18 presents the damaged zone as a function of the uniaxial compressive strength (f_c). The capability of the RHT model is to assess the damaged zone around the blast. It was found that the dimensions of the damaged zone increase for a decreased mechanical strength parameters of the rock mass (Fig. 18).

The assessment of the damaged zone remains important for the extractive industries, because it helps to determine the dimension of the bench and the amount of the fragmented rock, while performing production blasts. Based on the estimated damaged volume of the rock mass around the blast, the simulations will help to predict the dimension of the face burden to design. Hence, such model if useful to establish the design pattern of the production blast, as shown in Fig. 19.

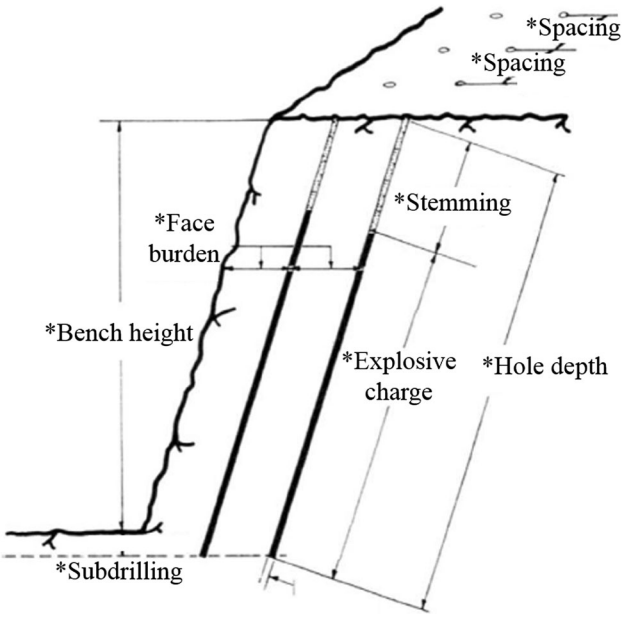

Fig. 19 Blast pattern parameters

Conclusion

An experimental study was carried out at the "*Sococim cement factory*," which is located in Senegal, in order to measure the three components of the blast-induced ground vibrations, namely the longitudinal (V_l), transverse (V_T) and vertical (V_v) velocity in three specific measuring

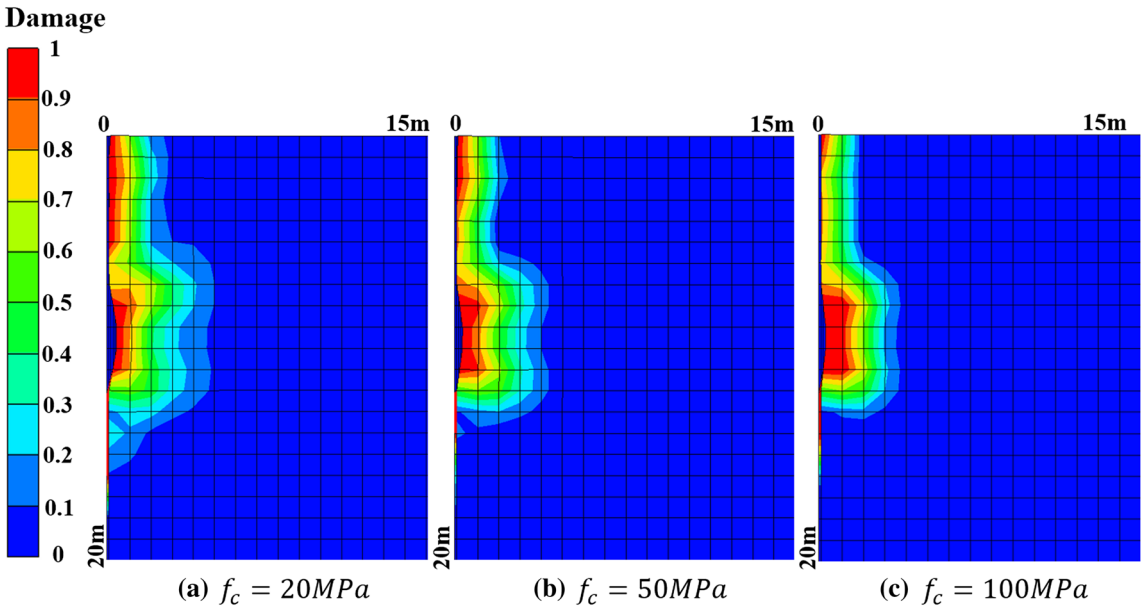

Fig. 18 Limestone's damage near the detonation point for $f_c = 20\,MPa$, $f_c = 50\,MPa$ and $f_c = 100\,MPa$

points: "*P1* (*Upper exploitation level*)," "*Macodo's house*" and "*Conveyor belt sites*." Three trial blasts were conducted using three equivalent TNT charges per delay ($m_{eq(TNT)}$), in particular 50 kg, 100 kg and 150 kg.

The special feature of this paper lies in the fact that the recorded experimental measurements of the trial blast series were used to validate our suggested two-dimensional axisymmetric model. The numerical modeling was developed under *AUTODYN* software, which is an explicit FEM code, commonly used to carry out nonlinear dynamics studies on solids, fluids and their interaction. The RHT model that was assigned to the rock mass yielded acceptable numerical results, because the trend of the numerical longitudinal and vertical velocity signals were similar to experimental results, although a slight difference was noted in the distribution of temporal signal's vibration.

The calibration was carried out on the elastic properties of the rock mass. Based on the tuned parameters (K and G), it has been found that the longitudinal and vertical PPV of the numerical results are in a good agreement with of the experimental measurements. In addition, the phenomenon of vibration's damping as a function of time at the gauges locations is well reproduced by the numerical model.

It has been found that the RHT model does not affect the celerity of the wave, which was slightly equivalent to the wave's celerity calculated analytically under the assumption of an elastic medium.

Among the major advantages of the RHT model is to assess the damaged zone around the blast. It has been found that the dimensions of the damaged zone increase for a decreased mechanical strength parameters of the rock mass. Based on the estimated damaged volume of the rock mass around the blast, the simulations will help to predict the dimension of the face burden to design. Therefore, the RHT model is necessary to establish the design pattern of the production blast.

Acknowledgements The authors wish to express their gratitude to "*Sococim company*" for good hospitality and cooperation.

Compliance with ethical standards

Conflict of interest The authors declare that they have no conflict of interest.

References

1. Afeni TB, Osasan SK (2009) Assessment of noise and ground vibration induced during blasting operations in an open pit mine—a case study on Ewekoro limestone quarry, Nigeria. Min Sci Technol (China) 19(4):420–424
2. AUTODYN: Theory manual. Century Dynamics (2006)
3. Coulombez C (2007) Analyse et optimisation des pratiques d'abattage a l'explosif dans une carrière de granulats
4. David ES, Stachura VJ, Stagg MS, Kopp JW (1980) Structure response and damage produced by ground vibration from surface mine blasting. Report of Investigations 8485, pp 1–112
5. Esmaeili M, Tavakoli B (2019) Finite element method simulation of explosive compaction in saturated loose sandy soils. Soil Dyn Earthq Eng 116:446–459. https://doi.org/10.1016/j.soildyn.2018.09.048
6. Hanchak S, Forrestal M, Young E, Ehrgott J (1992) Perforation of concrete slabs with 48 MPa (7 ksi) and 140 MPa (20 ksi) unconfined compressive strengths. Int J Impact Eng 12(1):1–7
7. Herrmann W (1969) Constitutive equation for the dynamic compaction of ductile porous materials. J Appl Phys 40(6):2490–2499
8. Holmquist TJ, Johnson GR (2011) A computational constitutive model for glass subjected to large strains, high strain rates and high pressures. J Appl Mech 78(5):051003
9. Hu Y, Chen L, Fang Q, Xiang H (2018) Blast loading model of the RC column under close-in explosion induced by the double end initiation explosive cylinder. Eng Struct 175:304–321. https://doi.org/10.1016/j.engstruct.2018.08.013
10. Iphar M, Yavuz M, Ak H (2008) Prediction of ground vibrations resulting from the blasting operations in an open-pit mine by adaptive neuro-fuzzy inference system. Environ Geol 56(1):97–107
11. Jehel P (2014) A critical look into Rayleigh damping forces for seismic performance assessment of inelastic structures. Eng Struct 78:28–40. https://doi.org/10.1016/j.engstruct.2014.08.003 (Performance Based Engineering: Current Advances and Applications)
12. Khandelwal M, Singh T (2006) Prediction of blast induced ground vibrations and frequency in opencast mine: a neural network approach. J Sound Vib 289(4):711–725. https://doi.org/10.1016/j.jsv.2005.02.044
13. Laine L, Sandvik A (2001) Derivation of mechanical properties for sand. In: Proceedings of the 4th Asia-Pacific conference on shock and impact loads on structures, CI-Premier PTE LTD, Singapore, vol 361. ANSYS Inc, p 368
14. Lee E, Finger M, Collins W (1973) JWL equation of state coefficients for high explosives. Technical report, Lawrence Livermore National Lab. (LLNL), Livermore, CA, USA
15. Li M, Zhu Z, Liu R, Liu B, Zhou L, Dong Y (2018) Study of the effect of empty holes on propagating cracks under blasting loads. Int J Rock Mech Min Sci 103:186–194. https://doi.org/10.1016/j.ijrmms.2018.01.043
16. Linforth S, Tran P, Rupasinghe M, Nguyen N, Ngo T, Saleh M, Odish R, Shanmugam D (2018) Unsaturated soil blast: flying plate experiment and numerical investigations. Int J Impact Eng. https://doi.org/10.1016/j.ijimpeng.2018.08.002
17. Lu W, Yang J, Chen M, Zhou C (2011) An equivalent method for blasting vibration simulation. Simul Model Pract Theory 19(9):2050–2062. https://doi.org/10.1016/j.simpat.2011.05.012
18. Maragakis E, Saiidi M, Abdel-Ghaffar S (1993) Response of r/c buildings during the 1987 whittier narrows earthquake. Earthq Spectra 9(1):67–95
19. Mohotti D, Ngo T, Raman SN, Mendis P (2015) Analytical and numerical investigation of polyurea layered aluminium plates subjected to high velocity projectile impact. Mater Des 82:1–17. https://doi.org/10.1016/j.matdes.2015.05.036
20. Murmu S, Maheshwari P, Verma HK (2018) Empirical and probabilistic analysis of blast-induced ground vibrations. Int J Rock Mech Min Sci 103:267–274. https://doi.org/10.1016/j.ijrmms.2018.01.038
21. Nateghi R (2012) Evaluation of blast induced ground vibration for minimizing negative effects on surrounding structures. Soil Dyn Earthq Eng 43:133–138. https://doi.org/10.1016/j.soildyn.2012.07.009

22. Ongen T, Karakus D, Konak G, Onur AH (2018) Assessment of blast-induced vibration using various estimation models. J Afr Earth Sci 145:267–273. https://doi.org/10.1016/j.jafrearsci.2018.05.004
23. Rao B, Chen L, Fang Q, Hong J, Xian LZ, Bo XH (2018) Dynamic responses of reinforced concrete beams under double-end-initiated close-in explosion. Def Technol 14(5):527–539. https://doi.org/10.1016/j.dt.2018.07.024
24. Riedel W (2000) Beton unter dynamischen lasten–meso-und makromechanische modelle und ihre parameter. forschungsergebnisse aus der kurzzeitdynamik. Fraunhofer Institut für Kurzzeitdynamik, Ernst-Mach-Institut, Freiburg
25. Riedel W, Kawai N, Kondo Ki (2009) Numerical assessment for impact strength measurements in concrete materials. Int J Impact Eng 36(2):283–293
26. Riedel W, Thoma K, Hiermaier S, Schmolinske E (1999) Penetration of reinforced concrete by beta-b-500 numerical analysis using a new macroscopic concrete model for hydrocodes. In: Proceedings of the 9th international symposium on the effects of munitions with structures, vol 315. Berlin-Strausberg, Germany
27. Saleh M, Edwards L (2015) Evaluation of soil and fluid structure interaction in blast modelling of the flying plate test. Comput Struct 151:96–114. https://doi.org/10.1016/j.compstruc.2015.01.010
28. Salvado FC, Tavares AJ, Teixeira-Dias F, Cardoso JB (2017) Confined explosions: the effect of compartment geometry. J Loss Prev Process Ind 48:126–144. https://doi.org/10.1016/j.jlp.2017.04.013
29. Sauer C, Heine A, Riedel W (2017) Developing a validated hydrocode model for adobe under impact loading. Int J Impact Eng 104:164–176. https://doi.org/10.1016/j.ijimpeng.2017.01.019
30. Shi Y, Stewart MG (2015) Spatial reliability analysis of explosive blast load damage to reinforced concrete columns. Struct Saf 53:13–25. https://doi.org/10.1016/j.strusafe.2014.07.003
31. Singiresu SR et al (1995) Mechanical vibrations, Addison Wesley
32. Tang EK, Hao H (2010) Numerical simulation of a cable-stayed bridge response to blast loads, part I: model development and response calculations. Eng Struct 32(10):3180–3192. https://doi.org/10.1016/j.engstruct.2010.06.007
33. Verma H, Samadhiya N, Singh M, Goel R, Singh P (2018) Blast induced rock mass damage around tunnels. Tunn Undergr Space Technol 71:149–158. https://doi.org/10.1016/j.tust.2017.08.019
34. Yi C, Sjöberg J, Johansson D (2017) Numerical modelling for blast-induced fragmentation in sublevel caving mines. Tunn Undergr Space Technol 68:167–173. https://doi.org/10.1016/j.tust.2017.05.030
35. Zeng Y, Li H, Xia X, Liu B, Zuo H, Jiang J (2018) Blast-induced rock damage control in Fangchenggang Nuclear Power Station, China. J Rock Mech Geotech Eng 10(5):914–923. https://doi.org/10.1016/j.jrmge.2018.04.010
36. Zhang QL, Li DY, Wang F, Li B (2018) Numerical simulation of nonlinear structural responses of an arch dam to an underwater explosion. Eng Fail Anal 91:72–91. https://doi.org/10.1016/j.engfailanal.2018.04.025
37. Zhao JJ, Zhang Y, Ranjith P (2017) Numerical simulation of blasting-induced fracture expansion in coal masses. Int J Rock Mech Min Sci 100:28–39. https://doi.org/10.1016/j.ijrmms.2017.10.015
38. Zhao X, Wang G, Lu W, Chen M, Yan P, Zhou C (2018) Effects of close proximity underwater explosion on the nonlinear dynamic response of concrete gravity dams with orifices. Eng Fail Anal 92:566–586. https://doi.org/10.1016/j.engfailanal.2018.06.016
39. Zhi X, Qi S, Fan F, Zhai X (2018) Experimental and numerical investigations of a single-layer reticulated dome subjected to external blast loading. Eng Struct 176:103–114. https://doi.org/10.1016/j.engstruct.2018.08.105
40. Zhu JB, Li YS, Wu SY, Zhang R, Ren L (2018) Decoupled explosion in an underground opening and dynamic responses of surrounding rock masses and structures and induced ground motions: a fem–dem numerical study. Tunn Undergr Space Technol 82:442–454. https://doi.org/10.1016/j.tust.2018.08.057